Large-Eddy Simulation of Flame Dynamics During the Ignition of a Swirling Injector Unit and Comparison With Experiments

Karl Töpperwien, Félix Collin-Bastiani, Eleonore Riber, Bénédicte Cuenot, Guillaume Vignat, Kevin Prieur, D. Durox, Sébastien Candel, Ronan Vicquelin

Large-Eddy Simulation of flame dynamics during the ignition of a swirling injector unit and comparison with experiments

Karl Töpperwien[1]*, Félix Collin-Bastiani[2,3], Eleonore Riber[2], Bénédicte Cuenot[2], Guillaume Vignat[1], Kevin Prieur[1,4], Daniel Durox[1], Sébastien Candel[1], Ronan Vicquelin[1]
[1]Laboratoire EM2C, CNRS, CentraleSupélec, Université Paris-Saclay, 8 - 10 Rue Joliot Curie, 91192 Gif-sur-Yvette cedex, France
[2]CERFACS, 42 Avenue Gaspard Coriolis, Toulouse Cedex 1 31057, France
[3]Safran Aircraft Engines, Rond Point René Ravaud, 77550 Moissy-Cramayel, France
[4]Safran Tech, E&P, Châteaufort, CS 80112, 78772 Magny-Les-Hameaux, France
Email: karl.topperwien@centralesupelec.fr

During the ignition of a swirled single-injector combustor, two phases have been identified experimentally. In the first, the flame penetrates the injection unit, while in the second the flame lifts off after a substantial delay before stabilizing at a distance from the injector. This transient phenomenon is investigated using Large Eddy Simulations based on an Euler-Lagrange description of the liquid spray, an energy deposition model to mimic ignition and the thickened flame combustion model. It is shown that the initial penetration of the flame in the injector unit is linked with the positive pressure excursion induced by the rapid volumetric expansion of burnt gases. This sudden expansion is itself due to the fast increase in heat release rate that occurs during the initiation of the process. The corresponding positive and negative pressure disturbances induce a rapid reduction of the mass flow rate through the injector, followed by an acceleration of the flow and a return to the nominal value. It is also shown that the flame root disappears after another delay, which results in the flame edge lifting and stabilization at a distance from the injector exhaust corresponding to steady operation of the device. The relatively long delay time before this lift-off takes place is found to correspond to the residence time of the cooled burnt gases in the vicinity of the chamber walls, which are ultimately entrained by the internal recirculation zone and quench the lower flame foot.

INTRODUCTION

A safe and reliable ignition of combustion chambers under a wide range of operating conditions is of vital importance for aeronautical applications and, more generally, for gas turbines. This can be a challenging task within the constraints set by emission legislation, lean overall equivalence ratios, strong local inhomogeneities and complex geometries. Aero-engine combustors are operated with liquid fuels which may cause additional difficulties for high altitude reignition when combustor temperatures and pressure are low and flow velocities are reduced, thus leading to poor fuel atomization and mixing. Research is therefore needed not only to better understand the phenomena which lead to successful ignition but also to avoid ignition failure and hardware damage that may be caused by inadequate management of the ignition transient.

Ignition is usually initiated by external forcing, e.g., a spark, although concepts for auto-igniting combustors exist in sequential or multi-staged stationary gas turbines [1, 2]. The classification into the following three phases of forced ignition has been well established in the literature [3, 4]: (1) Kernel generation, (2) Flame growth and stabilization and (3) Burner-to-burner flame propagation, called light-round ignition. Extensive research has therefore been dedicated to the characterization of a successful ignition process, including detailed investigations of spark characteristics such as the minimum spark energy [5], ignition probability and impact of turbulence [6, 7]. Moreover, to establish a successful flame growth and stabilization, the spark region must offer close to stoichiometric mixtures and flow velocities which do not avert an upstream propagation of the flame [8, 9]. When fuel is injected as a droplet spray, ignition and propagation may notably differ from the processes corresponding to purely gaseous flames. Concerning the ignition of spray flames, numerical studies performed in [10] highlight differences in the initial kernel structure as well as in the different possible modes of ignition. Flame propagation was found to depend on the droplet size distribution and the amount of prevaporized fuel [11]. This is confirmed for instance in [12] in which distinct propagation modes are identified. Moreover, an inverse correlation of the burning velocity with the Sauter Mean Diameter (SMD) is also demonstrated by Neophytou

*Address all correspondence to this author.

and coworkers [13] in a bluff-body configuration. This effect was primarily attributed to the increased time needed for the evaporation of large droplets.

Experimental data of light-round ignition in laboratory-scale annular combustors has become available more recently for premixed gaseous [14, 15] and non-premixed [16] systems. Burner spacing and overall equivalence ratio were identified to govern the propagation speed as well as the flow field resulting from the volumetric expansion across the flame. Numerical simulations of premixed [17] and non-premixed [18] annular configurations have proven, among others, that Large Eddy Simulations (LES) suitably retrieve experimental light-round trends. In the case of liquid fuel injection as a spray, numerical simulations have been successfully validated against experimental data becoming available recently for swirled annular spray-combustors using an Euler-Euler approach [19, 20] or Euler-Lagrange [21] approach for the liquid phase.

A recent work by Prieur et al. [22] offers experimental insights into the dynamic behavior of spray flames during the ignition transient which are less well documented in the previous literature. These recent data are of particular interest as the flame is found to flashback under certain conditions and might damage the injection unit eventually. Flame flashback has been known to occur, for example, due to thermo-acoustic instabilities [23–25] or transition between combustion regimes [26]. However, experimental measurements reported in [22] suggest that flashback events are also possible during the combustor ignition sequence.

The present investigation relies on experimental observations made in a single-injector configuration, the SICCA chamber, operated at the EM2C laboratory. High-speed imaging revealed that the flame penetrates the injector and is initially present in this unit. After a delay, the lower flame brush is quenched, initiating a flame lift-off before stabilization at a distance from the injector. During the same period, the flame is also observed to change its shape.

The objective of the present work is to complement the experimental data and gain further insight into the mechanisms that drive the dynamic behavior which has not been covered in previous numerical studies and cannot be readily measured experimentally. This is achieved by making use of LES.

The outline of this work is as follows: the setup of the SICCA combustor is briefly presented, followed by an overview of the employed models and the numerical setup. Results of the LES are analyzed subsequently and compared with available experimental data.

EXPERIMENTAL CONFIGURATION

The SICCA-combustor (Fig. 1) is a swirled, single-injector spray-combustor operated at ambient pressure. It is designed to facilitate the investigation of ignition phenomena occurring in aeronautical annular combustion chambers, allowing to characterize the flow aerodynamics, spray structure and flame geometry. The combustor features a pressurized simplex atomizer which feeds liquid fuel at 6 bar into

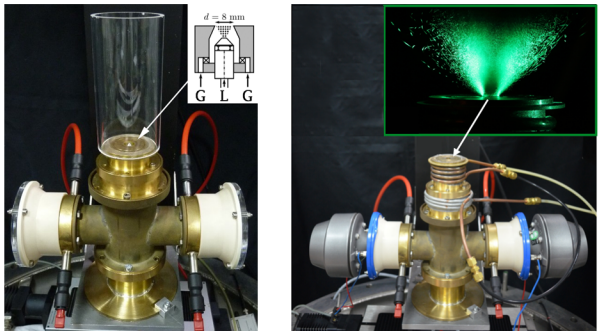

Fig. 1: Experimental setup of the SICCA combustor. Left: confined setup with a single injector unit. The atomizer is recessed with respect to the injector outlet. Right: unconfined setup for spray diagnostics with the atomizer mounted flush with the injector outlet.

the swirler (measured swirl number $S = 0.68$) where it mixes with air injected further upstream at the air inlets. The injector end piece has a conical shape with an outlet diameter of $d = 8$ mm. The fuel injector is mounted 6 mm in recess with respect to the injector outlet. In this configuration, a hollow-cone spray is released into the combustion chamber which is confined by a cylindrical quartz tube of 70 mm inner diameter, 150 mm height and 5 mm thickness. Under stationary conditions, a flame stabilizes at a distance from the swirler outlet. For ignition, a conventional spark plug is used which is positioned close to the combustor back-plane and eccentric with respect to the combustor symmetry axis.

Various spray diagnostics have been performed as well as high-speed imaging of the ignition sequence which are detailed in [22]. Wall temperature measurements are available at the nominal, steady-state operating point of the combustor which are imposed in the simulations.

MODELING AND NUMERICAL SETUP

In the present two-phase flow approach, the governing equations for each phase are integrated by the explicit flow solver AVBP (*www.cerfacs.fr/avbp7x*) [27] on an unstructured mesh. The most important numerical details and physical models are summarized in the following.

Gas phase

The filtered, compressible Navier-Stokes equations are solved for the gas phase. A two-step Taylor-Galerkin (TTGC, [27]) scheme (third order accuracy in space and time) is used to solve the conservation equations numerically. Sub-grid scale contributions are computed following the classical eddy viscosity assumption. The turbulent eddy viscosity is evaluated according to the SIGMA-model [28]. The turbulent species diffusivity and the turbulent heat conduction coefficient are determined from the turbulent Schmidt and Prandtl numbers (both equal to 0.6).

Dispersed phase

In this work, the liquid droplets are tracked in the Lagrangian framework. The governing equations for droplet motion are given as:

$$\frac{dx_{p,i}}{dt} = u_{p,i} \tag{1}$$

$$\frac{du_{p,i}}{dt} = \frac{f_{p,i}}{m_p} \tag{2}$$

with x_p, u_p and m_p denoting the droplet position, velocity and mass, respectively. The two-way coupling between the polydisperse liquid phase and the gaseous phase causing a drag-force f_p is taken into account by the Schiller-Naumann drag force model [29]. Phase interactions associated with evaporation are coupled in a similar manner via exchange terms in their respective mass and energy balances. Fuel addition to the gaseous phase and evaporative cooling are effectively represented by these terms. Unlike the conservation equations for the gaseous phase, a two-step Runge-Kutta scheme is used to integrate the dispersed phase equations which are coupled at every iteration to the gaseous solver.

Evaporation model

Due to droplet evaporation, additional equations are required to account for heat and mass transfer between the phases:

$$\frac{dm_p}{dt} = \dot{m}_p \tag{3}$$

$$\frac{dT_p}{dt} = -\frac{1}{m_p c_{p,l}} \phi_p^c \tag{4}$$

introducing the evaporation rate $\dot{m}_p$, the specific heat of the liquid $c_{p,l}$ and the conductive heat-flux ϕ_p^c. The well-known Spalding-model [30] provides expressions for $\dot{m}_p$ and heat fluxes in the gas phase ϕ_g^c which read as:

$$\dot{m}_p = -\pi d_p \, \mathrm{Sh} \, \rho_g D_g \ln(1 + B_M) \tag{5}$$

$$\phi_g^c = -\pi d_p \, \mathrm{Nu} \, \lambda (T_\infty - T_p) \frac{\ln(1+B_T)}{B_T} \tag{6}$$

where d_p, Sh, ρ_g, D_g, Nu and λ denote the droplet diameter, the Sherwood number, the density of the gaseous mixture, the diffusion coefficient of the gas phase, the Nusselt number and the thermal conductivity in the gas phase. The vapor film which forms around an evaporating droplet and modifies the mass and thermal transport is accounted for by the Spalding numbers of diffusive mass and thermal transport, B_M and B_T, evaluated according to the method of Abramzon and Sirignano [31].

For the evaluation of B_M under the assumption of thermodynamic equilibrium, the saturation pressure at the droplet surface is required which can be obtained from the Clausius-Clapeyron formula (pre-tabulated in AVBP). The Sherwood and Nusselt numbers follow from a correlation proposed by Frössling [32] which are functions of the droplet Reynolds number Re_p, the Prandtl number Pr_{film} and the Schmidt number Sc_{film} in the vapor film. Its thermal conductivity follows from $\lambda = \mu c_{p,g} / \mathrm{Pr}_{film}$. These properties are commonly evaluated at a reference state, which can be interpolated between far-field and droplet surface conditions by the "third-rule" [33].

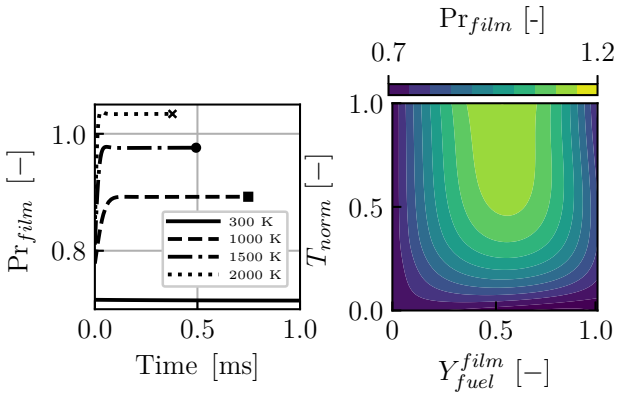

Fig. 2: Left: Temporal evolution of Pr_{film} during evaporation of a droplet of n-heptane in pure air at varying air temperatures. Solid line: $T_{air} = 300$ K, dashed: 1000 K, dash dotted line: 1500 K, dotted: 2000 K. Right: map of Pr_{film} calculated for generic droplet films.

A balance equation at the phase interface yields a relation for the conductive heat fluxes of each phase, given as:

$$\phi_p^c = -\phi_g^c + \dot{m}_p L_v(T_p) \tag{7}$$

For the evaluation of this equation, the latent heat of vaporization at the droplet temperature is needed which is read from lookup tables.

A critical task consists in the computation of the film properties D_g, μ and λ which depend on Pr_{film} and Sc_{film}. This has been outlined in detail very recently by Sacomano Filho and co-workers [34]. Considerable variations of these dimensionless numbers can be expected during the evaporation of a droplet. Reference data for droplet evaporation of n-heptane (droplet diameter $d_p = 15$ μm, droplet temperature $T_p = 300$ K) in pure, quiescent air computed with the EM2C in-house code AGATH are plotted in Fig. 2 (left). Each curve corresponds to a different surrounding air temperature to which the droplet is exposed. An increase of Pr_{film} can be observed with increasing air temperature while the evaporation time (indicated by markers) is decreasing. For Sc_{film} (not shown here), the trend with increasing surrounding air temperature is inverted. In addition, Pr_{film} appears to change over time in each case (the same holds for Sc_{film}). Further analysis of the droplet film reveals that the film composition and film temperature are modified during evaporation, hence the observed effect on Pr_{film} and Sc_{film}.

To assess the variations of the film dimensionless numbers, generic droplet films have been systematically calculated in Fig. 2 (right). This map visualizes the variation of Pr_{film} due to changes of the film composition, represented by the film fuel mixture fraction (Y_{fuel}^{film}) and film temperature, plotted in a normalized form as T_{norm} (normalization between $T_{min} = 280$ K and $T_{max} = 2400$ K). The film Prandtl number ranges between 0.7 and 1.2 within the given boundaries. Thus, an accurate description of droplet evaporation requires the computation of the droplet film properties which can be computationally expensive.

This has led to a method derived in [35] in which Pr_{film} and Sc_{film} are replaced by constants deduced from preliminary detailed 0D evaporation simulations. Very good results in terms of predicted evaporation time can be obtained in those cases in which the film properties can be expected to have little variation only, e.g. in stationary combustion.

During ignition, however, substantial variations in the droplet film can occur due to temperature and mixture fraction gradients which are encountered along the droplet trajectories and this may cause important discrepancies in the predicted droplet evaporation time. Therefore, an extended approach is proposed in this work. Instead of imposing constant values, Prandtl and Schmidt numbers are directly evaluated in AVBP as a function of the film temperature T_{film} and the film fuel mass fraction Y_{fuel}^{film}. In this method, Pr_{film} and Sc_{film} of generic droplet films are fitted with a third-order, bivariate polynomial function $\left(f\left(Y_{fuel}^{film}, T_{norm}\right)\right.$, normalization of $\left.T_{film}\right)$ using a least-square fit. Note that evaluating the film properties directly from detailed transport properties computation is also a solution but this would significantly increase the computational cost of the LES.

The corresponding fit coefficients are eventually implemented in AVBP and allow to use variable Prandtl and Schmidt numbers in the evaporation model as a function of the governing film properties. For efficient and numerically accurate evaluation of the polynomial function, Horner's rule [36] is applied.

To assess the accuracy of this approach, the error in droplet evaporation time t_{evap} is plotted as a function of the equivalence ratio ϕ_∞ and temperature T_∞ of the (far-field) gas phase in which a droplet of n-heptane is evaporating. Very good results can be obtained for the droplet evaporation time in pure air (max. error 3 %, see Fig. 3 (left)) and a still acceptable error of max. 8 % is made in burnt gases at high temperature (Fig. 3 (right)).

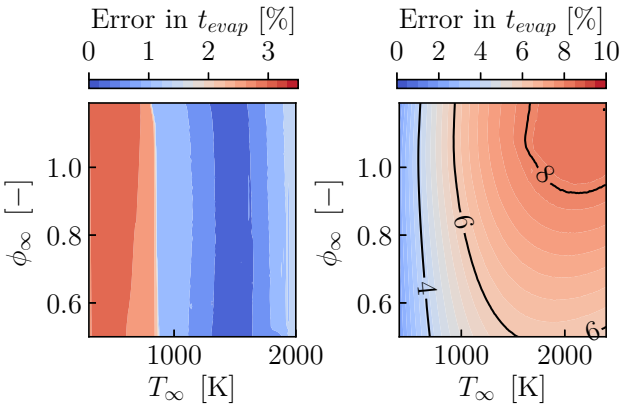

Fig. 3: A posteriori error assessment of the extended evaporation model as a function of temperature and equivalence ratio of the surrounding gas phase. Left: error in t_{evap} for evaporation of n-heptane in pure air. Right: error in t_{evap} for evaporation in burnt gases.

Fuel injection model

For the injection of liquid fuel, the phenomenological FIM-UR approach (Fuel Injection Method by Upstream Reconstruction, [37]) is employed. The injected droplet size distribution is represented by a Rosin-Rammler distribution parameterized by a shape parameter $q = 1.3$ and a diameter $d_{SMD} = 18$ μm to fit experimental data reported in [38]. The mean half-angle $\theta = 32^\circ$ is chosen to best fit experimentally measured velocity profiles in non-reacting conditions at 2.5 mm above the chamber backplane.

Assuming a dilute spray regime, droplet-droplet interactions are neglected which is verified a posteriori. Secondary atomization at the swirler exit is not yet covered.

Combustion model

A two-step, six species (C_7H_{16}, CO_2, CO, H_2O, O_2, N_2) global reaction scheme for n-heptane as proposed in [39] is used in this work. Reaction rates following the Arrhenius-law are corrected according to the methodology referred to as Pre-Exponential Adjustment (PEA) [40]. A validation against detailed schemes [41] has been performed in [39] proving a reasonably good prediction of the laminar burning velocity at ambient pressure and a wide range of equivalence ratios.

The interaction of the flame with turbulence on a subgrid-scale level is controlled by the Dynamic Thickened Flame Model (TF-LES, [42]). While this allows for a thin flame front to be resolved on a grid that is coarser than the flame thickness, an efficiency function E [43] with constant $\beta = 0.5$ is required to compensate for the decreased sensitivity of the thickened flame to subgrid-scale eddies. Note that due to the presence of a liquid phase, thickening is also applied on drag and evaporation [39]. A flame sensor based on a lagrangian flame-front tracking approach as proposed in [44] is employed.

Numerical domain and boundary conditions

Figure 4 shows the numerical domain, a vertical mesh-cut of the swirler and the lower part of the combustion chamber as well as a cut-plane perpendicular to the swirler. This mesh has already been used for validation purposes in a non-reacting as well as in a reactive, steady-state operation [21]. The mesh covers the entire air plenum, the swirler, the com-

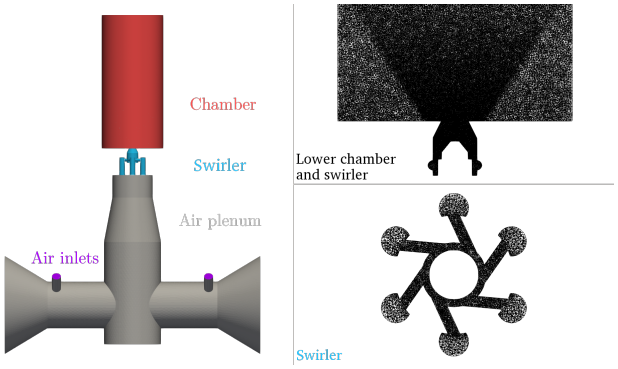

Fig. 4: Left: numerical domain (without ambient atmosphere). Top right: central mesh-cut of the injector and lower part of the chamber. Bottom right: mesh-cut of the swirler.

bustion chamber and a large cylinder representing the surrounding atmosphere (not shown in Fig. 4). Typical mesh sizes in the flame region are of the order of 0.4 mm.

For inlets and outlets, the Navier-Stokes Characteristic Boundary Conditions (NSCBC, [45]) are applied. Mass flow rates are imposed at the air inlet ($\dot{m}_{air} = 1.94$ g.s^{-1}) and the fuel inlet ($\dot{m}_{fuel} = 0.111$ g.s^{-1}) yielding a global equivalence ratio of $\phi_{glob} = 0.856$. All inlet temperatures are set to $T = 300$ K.

No-slip walls are assumed for the gas phase in the entire domain with the only exception being the swirler walls for which a wall-law is used. Liquid phase boundary conditions are set to allow elastic rebound in the combustion chamber. In the injector, droplet-wall interactions are considered to be predominant and require a film-type boundary condition.

Previous works on the same combustor have highlighted the importance of an accurate representation of the thermal boundary conditions in terms of flame dynamics and flame shapes [46]. Therefore, the experimentally measured wall temperature profile is imposed on the inner combustor walls, while all other walls upstream of the fuel injector are adiabatic. The water-cooled combustor backplane is kept at a temperature of $T = 410$ K. These conditions can be considered to emulate relight conditions immediately after flameout.

Initial conditions and ignition procedure

The two-phase flow field has been converged by first running a non-reactive simulation to reach the targeted global equivalence ratio in the ignition zone of the chamber. In contrast to [21], the wall temperature profile is imposed *ab initio* to ensure the convergence of the total heat flux across the chamber wall and backplane, i.e. steady-state conditions.

This initial solution is eventually ignited using a 1-step energy deposition model (ED) as developed in [47] to approximate the energy profile that a real spark would deliver, without simulating the initial plasma-phase. A volumetric source term is temporarily added to the energy equation featuring a Gaussian distribution in space and time. The center of the spherical energy source is positioned close to the combustor backplane in the outer recirculation zone (total energy $E = 70$ mJ, diameter $d = 11$ mm).

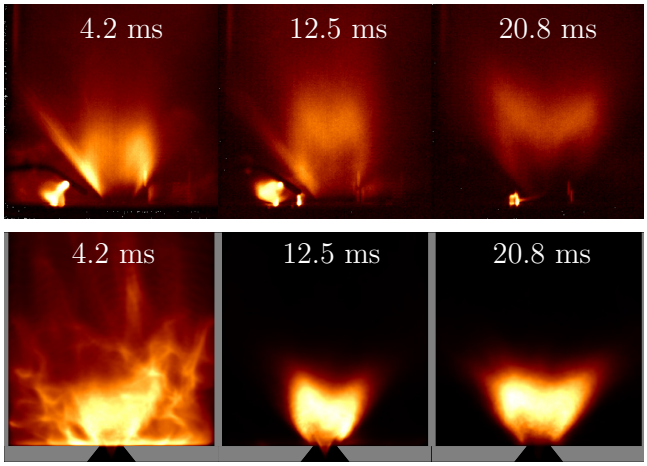

Fig. 5: Top: Experimental ignition sequence recorded by high-speed imaging (reprinted from [22]). Bottom: Simulated ignition sequence: line-of-sight integrated heat release rate.

IGNITION IN RELIGHT CONDITIONS

Three ignition sequences have been recorded with a high-speed camera [22] at the same nominal conditions out of which one is used as a reference. Figure 5 (top) shows the experimental images which were averaged over 8.3 ms centered around the respective time instant. Two distinct flame configurations can be identified: during the first two instances, the flame is attached to the injector outlet which can be referred to as shape *A* (adopting the terminology in [22]). In the last instance, a flame detached from the swirler can be observed assuming shape *B*. Figure 5 (bottom) illustrates the simulated ignition sequence as a line-of-sight integration of the heat release rate inside the combustion chamber and the swirler nozzle. The same temporal averaging has been performed on the numerical data as in the experimental case. Similar flame configurations are found numerically supporting the argument of a dynamic flame behavior during ignition. The numerical images clearly reveal a flashback during the first two instances (shape *A*) as the lower flame brush is anchored inside the swirler nozzle which is particularly difficult to record experimentally without direct optical access. Conversely, in the following instance, the lower flame brush appears to be entirely extinguished. Therefore, complementary to the definition of the two flame shapes, the initial period will be defined as flashback phase (flame shape *A*) and the second period as lift-off phase (flame shape *B*) in the remainder of this work. Note that flashback and liftoff phases are considered to appear within the flame propagation phase (2) of the general definition of forced ignition mentioned in the introduction [3]. Each phase will be analyzed separately in the following sections.

Flashback phase

The volume integrated heat release rate inside the combustion chamber sampled during the ignition sequence is visualized in Fig. 6 (top, line with bullet markers). A short and intense peak of the heat release rate of $\dot{Q} \approx 100$ kW can be observed during the consumption of the fresh gases inside the combustion chamber and a fast decay to the nominal thermal power of the combustor at 5 kW. The rapid expansion of burnt gases induces a pressure perturbation that is propagating through the combustor and, more importantly, upstream through the swirler into the air plenum as well. In Fig. 6 (top) the pressure signal fluctuation P' is monitored at the swirler inlet and the center of the combustion chamber. As the peak duration of these two signals overlap almost perfectly during the increase of the heat release rate, the effect of the burnt gas expansion on the pressure field can be considered to be immediate inside the entire combustor.

This relation between pressure and heat release is important for the analysis of mass flow rates which are recorded at the injector outlet and upstream in the air plenum in Fig. 6 (bottom). In fact, the pressure perturbation during the burnt gas expansion modulates the mass flow rates upstream of the combustion chamber, that is, at the injector exit (fresh gas mass flow rate) and in the air plenum (pure air mass flow rate): during sustained high pressure fluctuation levels, mass flow rates decrease substantially (cf. light gray areas in Fig. 6). Due to the temporary decrease of the mass flow rates the lower flame brush is able to propagate in the upstream direction and penetrates into the injector which is shown in detail in Fig. 7 (top) in the central cut-plane of the combustor. However, the lower flame brush detaches from the injector immediately after that moment, since the mass flow rates overshoot their respective average values at $t = 3.9$ ms (peak immediately after the gray area). Upon the subsequent drop of the mass flow rates due to another pressure peak at $t = 4.6$ ms (marked by a cross in Fig. 6) the flame is able to re-enter the injector up to the atomizer and find a stable configuration inside this unit. This process is illustrated in Fig. 7 (bottom).

In order to understand why this flame configuration remains stable despite further fluctuations of pressure and mass flow rates, it is instructive to examine the flow field and temperature distribution in the Internal Recirculation Zone (IRZ) as shown in Fig. 8 corresponding to the central cut-plane of the combustor. The flame front is visualized as black contour lines of heat release and the IRZ is surrounded by gray contour lines of zero axial velocity emerging from the swirler exit. The left image corresponds to a snapshot at $t = 3.3$ ms (sustained peak pressure), the right image to the reattached flame configuration at $t = 4.6$ ms discussed earlier. In the second image, the IRZ entrains burnt gases at higher temperature compared to the preceding snapshot. This leads to high temperature combustion products being fed into the lower flame brush facilitating flame stabilization inside the injector.

With this result in mind, the question might be raised, whether the energy profile introduced in the simulation, the ignition method itself or even the presence of a liquid phase might intensify the pressure excursion in an inappropriate manner leading to a flame flashback which would not have appeared otherwise. While experimental data of a purely gaseous configuration prove that the flashback process also accompanies ignition independently of the presence of the liquid phase (see Appendix of [22]), additional data can also be provided to assess the impact of the ignition method. Instead of using the energy deposition model for ignition, a simplified approach can be used by locally replacing the fresh gas mixture at the position of the igniter by burnt gases. In order to compare this method to the energy deposition approach, a separate simulation has been carried out from the exact same initial conditions. Ignition is achieved by introducing a sphere of burnt gases with the same dimensions ($d = 11$ mm) at the same position as in the energy deposition case to preserve consistency. In this manner, a spherical heat release profile is initialized which corresponds to a laminar, adiabatic flame at the local composition. The resulting simulated evolution of the heat release rate profile as well as the corresponding pressure signal at the center of the combustion chamber is plotted in Fig. 9. The corresponding profiles of the energy deposition method (already shown in Fig. 6) are added to facilitate the comparison. As expected, the volume integrated heat release rate profiles are quite similar in both cases and induce similar pressure signals, although with a steeper initial transient in the case of the energy deposition model. Nevertheless, the same dynamical behavior (flashback and subsequent lift-off) can be observed (not shown here) even with a simplified ignition approach. Thus, the major conclusion that can be drawn from the previous discussion is that the flame flashback occurs independently from the kernel initialization method. In the context of this work, the main purpose of the initialization method is to deliver an appropriate flame kernel which does not require an explicit modeling of the very first flame initiation after the plasma-phase to reproduce the pressure evolution in the combustion chamber which eventually causes the flashback.

Lift-off phase

After the flame stabilization during the flashback phase, this configuration prevails for a total of 14 ms before transitioning into shape *B*. This transition is shown in the central cut-plane of the combustor in Fig. 10. Starting from the anchored position (Fig. 10 (left)), the flame splits into an upper and lower flame branch (Fig. 10 (center)). The lower branch shrinks and completely vanishes as the transition into shape *B* takes place. The flame is finally detached from the swirler (Fig. 10 (right)).

The characteristic delay time before the onset of this process is relatively long and may be linked to the cooling of the burnt gases that circulate in the vicinity of the combustor walls as will be shown in what follows. Between $t = 8.7$ ms and $t = 15.4$ ms (cf. light gray area in Fig. 11), the burnt gas temperature in the Outer Recirculation Zone (ORZ) is substantially reduced from 2400 K to around 1500 K due to cooling by the combustor walls. By contrast, the temperature in the IRZ remains nearly constant until the lower flame

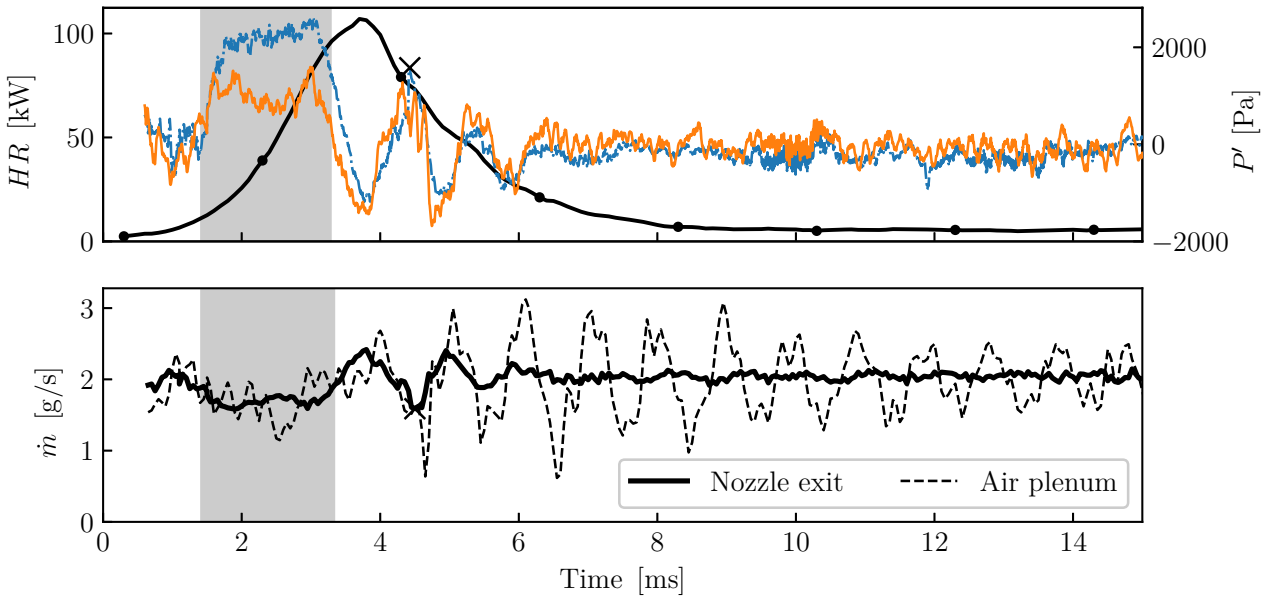

Fig. 6: Top: volume integral of chamber heat release rate (solid line with bullet markers) and pressure signal sampled at the center of the combustor (dash dotted line) and at the injector outlet (solid line). Bottom: mass flow rates in the simulation at the injector outlet (thick line) and inside the air plenum (thin dashed line).

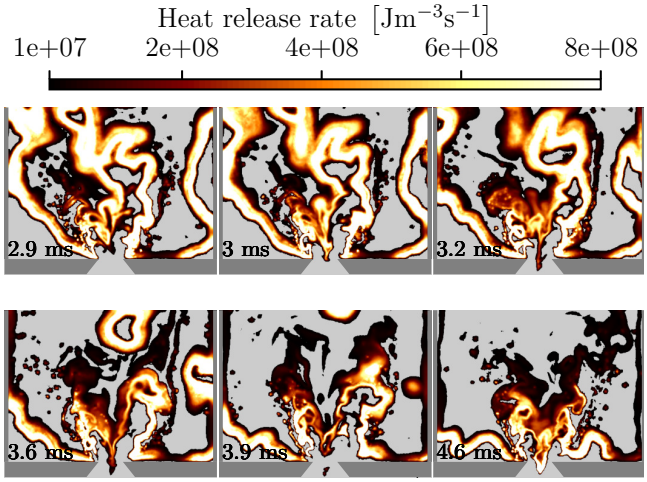

Fig. 7: Instantaneous heat release rate on the central cut-plane of the combustor during the initial sustained high pressure levels (top) and during the second drop of the mass flow rates (bottom).

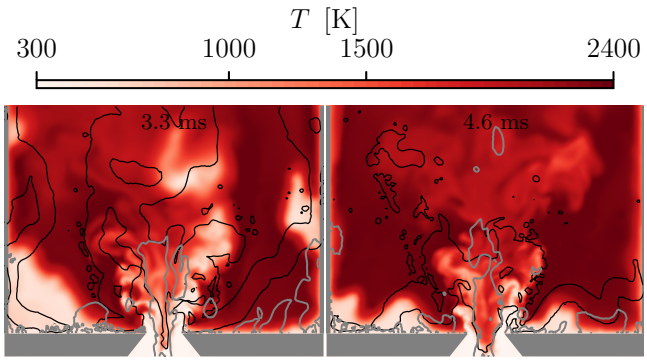

Fig. 8: Instantaneous gas temperature in the central axial plane through the combustion chamber. Black contour lines correspond to a heat release rate of 10^8 Jm^{-3}s^{-1}, gray contours to zero axial velocity.

branch splits and quenches resulting in a steep temperature decrease in the IRZ (cf. dark gray area in Fig. 11).

However, a heat loss effect in the IRZ which is suggested here as the driving mechanism for the flame lift-off cannot be directly inferred from the temperature signals because no differentiation can be made locally between fresh and burnt gases. For this reason, a qualitative index is introduced to visualize the heat losses from the burnt gases. This index I_{HL} is defined as a normalized enthalpy, written as:

$$I_{\mathrm{HL}} = \frac{h - h_l}{h_a - h_l} \in [0,1] \tag{8}$$

where h is the local enthalpy value, h_a the adiabatic enthalpy at the local composition and h_l the enthalpy of the local composition at the lowest temperature in the chamber, which is deliberately set to the lowest wall temperature inside the combustion chamber $T = 410$ K. When I_{HL} is unity, adiabatic conditions prevail in the local composition, while

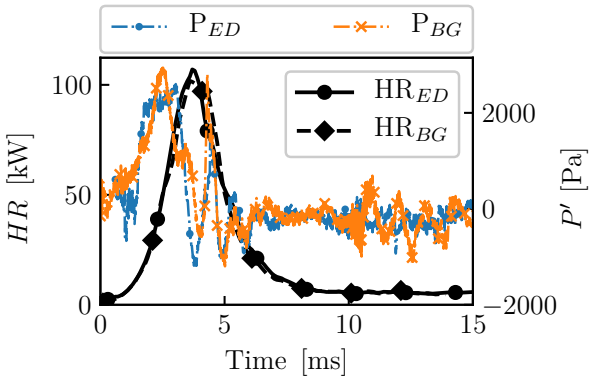

Fig. 9: Volume integrated heat release rate using the energy deposition model (subscript ED, solid line, bullet markers) and a simplified burnt gases approach (subscript BG, dashed line, diamond markers). The corresponding pressure evolutions at the center of the combustion chamber are represented by dash-dotted lines.

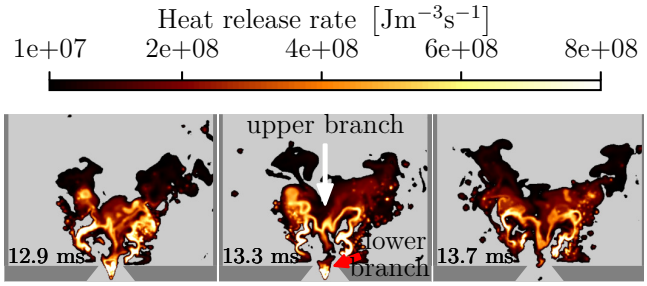

Fig. 10: Instantaneous heat release rate in the central axial plane of the combustor during flame lift-off and transition from shape *A* to *B*.

$I_{HL} = 0$ refers to the lowest enthalpy that a given composition may reach due to heat transfer to the chamber walls (i.e. highest heat loss). The heat loss index I_{HL} distribution in the central cut-plane through the combustor is shown in Fig. 12 after stabilization of the flame inside the injector (a) and during the transition from shape *A* to *B* (b-d). The flame is represented by black contour lines of iso-heat release rate, whereas gray contour lines mark regions of zero axial velocity. Note that the value range of I_{HL} is intentionally clipped between 0 and 1, although the fresh gas mixture before ignition can take values of $I_{HL} > 1$. This is only due to the fact that the fresh gases are heated by the combustor walls in the absence of combustion, resulting in higher enthalpy levels compared to a reference value which is (deliberately) set to the lowest temperature in the combustor. The same applies for burnt gases immediately after ignition and flame stabilization which is shown in Fig. 12(a). Contrary to the adiabatic flame and large parts of burnt gases that are in adiabatic

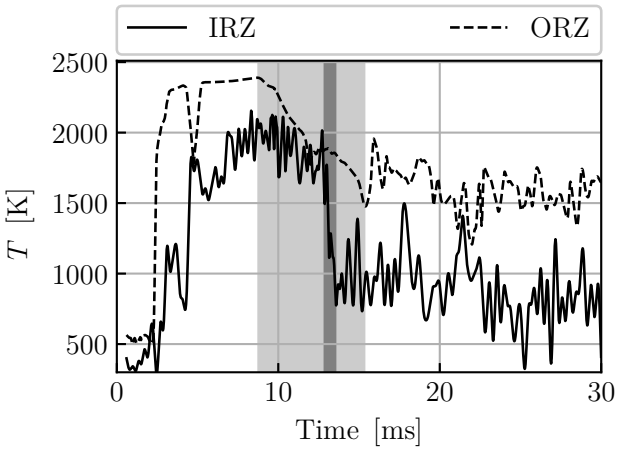

Fig. 11: Temporal evolution of temperature recorded in the IRZ and ORZ. The IRZ temperature signal is low-pass filtered (linear phase filter) for clearer identification of the curves.

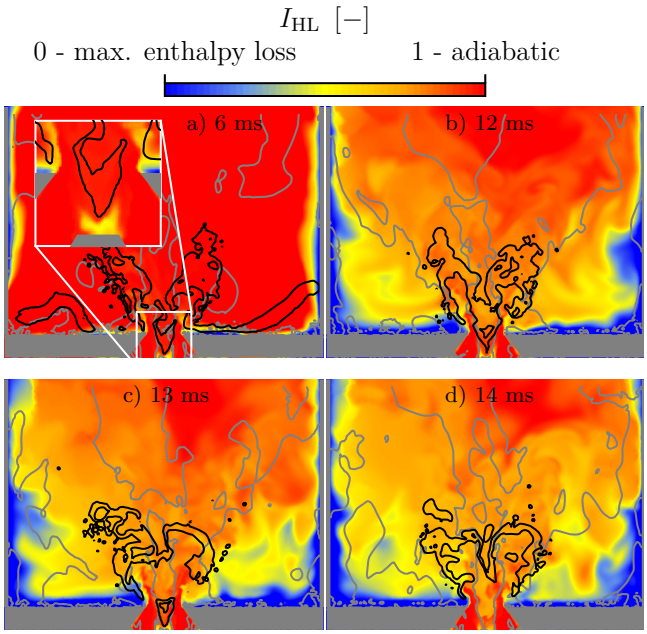

Fig. 12: Heat-loss index I_{HL} in the central axial plane through the combustion chamber. Black contour lines correspond to a heat release rate of 4×10^8 Jm^{-3}s^{-1}, gray contours to zero axial velocity.

conditions in the center of the combustion chamber which are not yet impacted by heat losses at this stage, near-wall fluid is constantly cooled by the combustor walls and I_{HL} is close to zero in this region. In the ORZ, flow velocities are comparably low (on the order of 15 m.s^{-1}) leading to a long exposure time of burnt gases to the walls. A substantial decrease of enthalpy starting in the ORZ and expanding downstream along the chamber walls can therefore be observed (Fig. 12(b-d)).

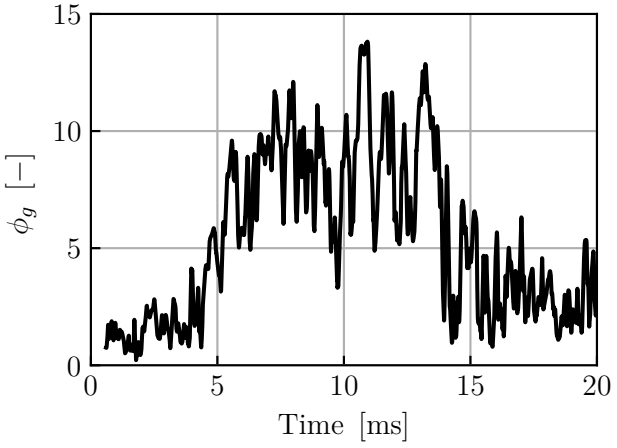

Fig. 13: Gaseous equivalence ratio ϕ_g sampled inside the injector above the fuel atomizer at $x = -0.005$ mm relative to the chamber backplane.

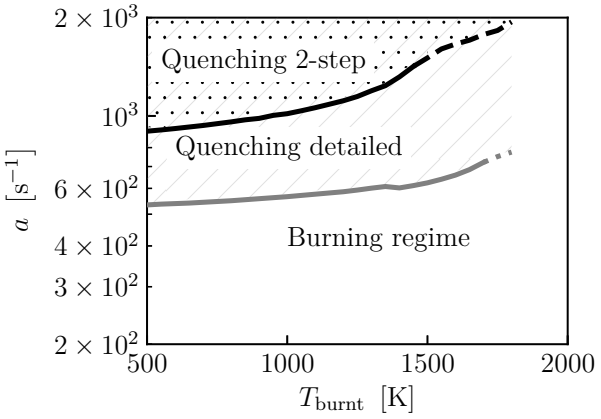

Fig. 14: Regime diagram of a counterflow flame. Thick solid lines mark the critical point of extinction for a given temperature for each reaction mechanism. Dashed and dotted line continuations indicate conditions where extinction and autoignition critical points collapse.

The flame is affected in the same manner, since cooled burnt gases are transported back upstream to the flame zone by the ORZ. Mixing again with fresh gases then results in a lower enthalpy of the combustion products leading to $I_{\mathrm{HL}} < 1$ even in the flame zone.

It may also be possible that the flame lift-off is locally enhanced by evaporative cooling of the gas phase close to the atomizer. The temporal evolution of the gaseous equivalence ratio ϕ_g inside the injection unit in Fig. 13 suggests that when the flame anchors inside the injector, evaporation is intensified causing a substantial increase of ϕ_g. Consequently, the gas phase locally incurs additional heat losses (cf. inset in Fig. 12(a)) and this may accelerate the extinction of the lower flame brush. However, evaporative cooling does not seem to have a first order impact on the flame lift-off as proven experimentally in a purely gaseous configuration (cf. [22, Appendix]), but may alter the transition time from the flashback to the lift-off phase.

Therefore, the flame lift-off can be explained more effectively by considering wall heat-losses: the IRZ which feeds the lower flame brush and sustains the initial flashback entrains burnt gases of decreasing enthalpy. As soon as the enthalpy is not sufficient to maintain a steady flame, the lower flame branch disintegrates and quenches entirely. The flame then stabilizes with a leading edge detached from the swirler.

A final discussion is dedicated to the impact of the two-step reaction mechanism on the prediction of quenching of the lower flame brush quenching. It is known that reduced kinetic mechanisms are less sensitive to strain rate and that in turn may delay quenching and lift-off. This issue is assessed by comparing the different flame regimes for the employed two-step mechanism and for a detailed mechanism for n-heptane (65 species, 315 reaction [41]).

Data is obtained by performing steady-state 1D simulations of stabilized counterflow flames with the code AGATH. The flow configuration is chosen such that the fuel side represents the fresh gas composition at ϕ_{glob} while the opposing stream side is formed by the corresponding burnt gas composition. Each 1D simulation is performed for a different set of imposed strain rate a and burnt gas temperature T_{burnt}. In the resulting regime diagram plotted in Fig. 14, quenching occurs in the hatched region for the detailed reaction mechanism whereas the dotted region corresponds to quenching predicted by the two-step reaction mechanism. Conversely, a steady flame can be established in the region marked as *burning regime*.

This comparison may be used to assess the flame lift-off observed in the SICCA-combustor in terms of the employed combustion chemistry. While both schemes show similar trends for flame extinction at low burnt gas temperatures and high strain rates, the quenched regime of the detailed mechanism extends towards higher temperatures and lower strain rates than the two-step mechanism. Thus, as the temperature of the IRZ decreases over time (cf. Fig. 11) the lower flame brush might extinguish at an earlier stage with detailed chemistry compared to the two-step mechanism.

CONCLUSION

The present work is focused on the transient dynamical processes that occur during the ignition of a swirling injector in a well-controlled laboratory-scale configuration. The injector offers an idealized version of practical systems used in aero-engines. The investigation is motivated by prior experimental observations in a multi-burner annular combustion chamber, indicating that flame flashback occurs during ignition followed by a final stabilization as a flame detached from the injection unit. This behavior is also retrieved in a single sector combustor equipped with one injector and characterized experimentally. This single-injector geometry is stud-

ied in this work using Large Eddy Simulations employing a polydisperse Euler-Lagrange formalism. The simulation suitably retrieves the two periods identified experimentally. During an initial period, the flame is attached to the chamber bottom with a lower flame brush anchoring inside the swirling injector. An analysis of pressure signals inside the combustion chamber and on the upstream side of the swirler indicates a strong transient perturbation of the pressure field which is related to the rapid expansion of the burnt gases inside the chamber. This pressure perturbation controls the mass flow rates of fresh gases at the injector outlet and even further upstream in the air plenum and leads to a temporary decrease of their respective levels. The flame is entrained by the internal recirculation zone which allows for an upstream propagation and eventually stabilizes inside the injector unit. This transient flashback during ignition highlights the potentially detrimental effect on the injector elements. The final stabilization in the form of a flame detached from swirler is found to be controlled by heat transfer taking place between recirculating burnt gases in the vicinity of the combustor walls. A heat-loss index defined as a normalized enthalpy calculated at different instants during the simulation reveals a continuous enthalpy decrease starting in the outer recirculation zone and gradually impacting the flame zone as the cooled burnt gases mix upstream with the fresh stream of reactants. Consequently, the internal recirculation zone progressively entrains colder combustion products and quenches the lower flame root that is initially located inside the injector. Finally, the flame detaches from the injection unit and takes its steady-state position with a leading edge separated from the swirler.

Acknowledgements

This project has received funding from the European Union's Horizon 2020 research and innovation program under the Marie Skłodowska-Curie grant agreement No 766264. Furthermore, the work was performed using HPC resources from GENCI-CINES (Grant 2018-A0042B10118) as well as from the "Mésocentre" computing center of CentraleSupélec and École Normale Supérieure Paris-Saclay supported by CNRS and Région Île-de-France (http://mesocentre.centralesupelec.fr/).

References

[1] Schulz, O., and Noiray, N., 2018. "Autoignition flame dynamics in sequential combustors". *Combustion and Flame,* ***192***, pp. 86–100.

[2] Ebi, D., Doll, U., Schulz, O., Xiong, Y., and Noiray, N., 2019. "Ignition of a sequential combustor: Evidence of flame propagation in the autoignitable mixture". *Proceedings of the Combustion Institute,* ***37***(4), pp. 5013–5020.

[3] Lefebvre, A. H., and Ballal, D. R., 2010. *Gas turbine combustion: alternative fuels and emissions*. CRC Press.

[4] Mastorakos, E., 2009. "Ignition of turbulent non-premixed flames". *Progress in Energy and Combustion Science,* ***35***(1), pp. 57–97.

[5] Ballal, D. R., and Lefebvre, A. H., 1975. "The influence of flow parameters on minimum ignition energy and quenching distance". *Symposium (International) on Combustion,* ***15***(1), pp. 1473–1481.

[6] Ahmed, S. F., Balachandran, R., Marchione, T., and Mastorakos, E., 2007. "Spark ignition of turbulent non-premixed bluff-body flames". *Combustion and Flame,* ***151***(1-2), pp. 366–385.

[7] Esclapez, L., Riber, E., and Cuenot, B., 2015. "Ignition probability of a partially premixed burner using les". *Proceedings of the Combustion Institute,* ***35***(3), p. 3133–3141.

[8] Cordier, M., Vandel, A., Cabot, G., Renou, B., and Boukhalfa, A. M., 2013. "Laser-induced spark ignition of premixed confined swirled flames". *Combustion Science and Technology,* ***185***(3), pp. 379–407.

[9] Sitte, M. P., Bach, E., Kariuki, J., Bauer, H. J., and Mastorakos, E., 2016. "Simulations and experiments on the ignition probability in turbulent premixed bluff-body flames". *Combustion Theory and Modelling,* ***20***(3), pp. 548–565.

[10] Neophytou, A., Mastorakos, E., and Cant, R. S., 2012. "The internal structure of igniting turbulent sprays as revealed by complex chemistry DNS". *Combustion and Flame,* ***159***(2), pp. 641–664.

[11] Ballal, D., and Lefebvre, A., 1981. "Flame propagation in heterogeneous mixtures of fuel droplets, fuel vapor and air". *Symposium (International) on Combustion,* ***18***(1), pp. 321–328.

[12] de Oliveira, P. M., and Mastorakos, E., 2019. "Mechanisms of flame propagation in jet fuel sprays as revealed by OH/fuel planar laser-induced fluorescence and OH* chemiluminescence". *Combustion and Flame,* ***206***, pp. 308–321.

[13] Neophytou, A., Richardson, E. S., and Mastorakos, E., 2012. "Spark ignition of turbulent recirculating non-premixed gas and spray flames: A model for predicting ignition probability". *Combustion and Flame,* ***159***(4), pp. 1503–1522.

[14] Bourgouin, J. F., Durox, D., Schuller, T., Beaunier, J., and Candel, S., 2013. "Ignition dynamics of an annular combustor equipped with multiple swirling injectors". *Combustion and Flame,* ***160***(8), pp. 1398–1413.

[15] Machover, E., and Mastorakos, E., 2017. "Experimental investigation on spark ignition of annular premixed combustors". *Combustion and Flame,* ***178***, pp. 148–157.

[16] Machover, E., and Mastorakos, E., 2016. "Spark ignition of annular non-premixed combustors". *Experimental Thermal and Fluid Science,* ***73***, pp. 64–70.

[17] Philip, M., Boileau, M., Vicquelin, R., Riber, E., Schmitt, T., Cuenot, B., Durox, D., and Candel, S., 2015. "Large Eddy Simulations of the ignition sequence of an annular multiple-injector combustor". *Proceedings of the Combustion Institute,* ***35***(3),

pp. 3159–3166.

[18] Machover, E., and Mastorakos, E., 2017. "Numerical Investigation of the Stochastic Behavior of Light-Round in Annular Non-Premixed Combustors". *Combustion Science and Technology,* ***189***(9), pp. 1467–1485.

[19] Boileau, M., Staffelbach, G., Cuenot, B., Poinsot, T., and Bérat, C., 2008. "LES of an ignition sequence in a gas turbine engine". *Combustion and Flame,* ***154***(1-2), pp. 2–22.

[20] Lancien, T., Prieur, K., Durox, D., Candel, S., and Vicquelin, R., 2017. "Large Eddy Simulation of Light-Round in an Annular Combustor With Liquid Spray Injection and Comparison With Experiments". *Journal of Engineering for Gas Turbines and Power,* ***140***(2).

[21] Collin-Bastiani, F., 2019. "Modeling and Large Eddy Simulation of Two-Phase Ignition in Gas Turbines". Phd thesis, Institut National Polytechnique de Toulouse.

[22] Prieur, K., Vignat, G., Durox, D., Schuller, T., and Candel, S., 2019. "Flame and spray dynamics during the light-round process in an annular system equipped with multiple swirl spray injectors". *Journal of Engineering for Gas Turbines and Power,* ***141***(6).

[23] Keller, J. O., Vaneveld, L., Ghoniem, a. F., Daily, J. W., Oppenheim, a. K., Korschelt, D., and Hubbard, G. L., 1981. "Mechanism of instabilities in turbulent combustion leading to flashback". *AIAA Journal,* ***20***(2), pp. 254–262.

[24] Lieuwen, T., McDonell, V., Petersen, E., and Santavicca, D., 2006. "Fuel Flexibility Influences on Premixed Combustor Blowout, Flashback, Autoignition and Instability". In Volume 1: Combustion and Fuels, Education, Vol. 2006, ASME, pp. 601–615.

[25] Schulz, O., Doll, U., Ebi, D., Droujko, J., Bourquard, C., and Noiray, N., 2019. "Thermoacoustic instability in a sequential combustor: Large eddy simulation and experiments". *Proceedings of the Combustion Institute,* ***37***(4), pp. 5325–5332.

[26] Sommerer, Y., Galley, D., Poinsot, T., Ducruix, S., Lacas, F., and Veynante, D., 2004. "Large eddy simulation and experimental study of flashback and blow-off in a lean partially premixed swirled burner". *Journal of Turbulence,* ***5***.

[27] Colin, O., and Rudgyard, M., 2000. "Development of High-Order Taylor-Galerkin Schemes for LES". *Journal of Computational Physics,* ***162***(2), pp. 338–371.

[28] Nicoud, F., Toda, H. B., Cabrit, O., Bose, S., and Lee, J., 2011. "Using singular values to build a subgrid-scale model for large eddy simulations". *Physics of Fluids,* ***23***(8).

[29] Schiller, L., and Naumann, A., 1935. "A drag coefficient correlation". *Zeitschrift des Vereins Deutscher Ingenieure,* ***77***, pp. 318–320.

[30] Spalding, D. B., 1953. "The combustion of liquid fuels". *Symposium (International) on Combustion,* ***4***(1), pp. 847–864.

[31] Abramzon, B., and Sirignano, W. A., 1989. "Droplet vaporisation model for spray combustion calculations". *International Journal of Heat and Mass Transfer,* ***32***(9), pp. 1605–1618.

[32] Frössling, N., 1938. "Über die Verdunstung fallender Tropfen (On the evaporation of falling drops)". *Gerlands Beiträge zur Geophysik,* ***52***, pp. 170–216.

[33] Hubbard, G. L., Denny, V. E., and Mills, A. F., 1975. "Droplet Evaporation: Effects of Transients and Variable Properties". *International Journal of Heat and Mass Transfer,* ***18***, pp. 1003–1008.

[34] Sacomano Filho, F. L., Krieger Filho, G. C., van Oijen, J. A., Sadiki, A., and Janicka, J., 2019. "A novel strategy to accurately represent the carrier gas properties of droplets evaporating in a combustion environment". *International Journal of Heat and Mass Transfer,* ***137***, pp. 1141–1153.

[35] Hannebique, G., Sierra, P., Riber, E., and Cuenot, B., 2013. "Large eddy simulation of reactive two-phase flow in an aeronautical multipoint burner". *Flow Turbulence and Combustion,* ***90***(2), pp. 449 – 469.

[36] Horner, W. G., 1819. "A New Method of Solving Numerical Equations of All Orders by Continuous Approximation". *Philosophical Transactions of the Royal Society of London,* ***109***, pp. 308–335.

[37] Sanjosé, M., Senoner, J. M., Jaegle, F., Cuenot, B., Moreau, S., and Poinsot, T., 2011. "Fuel injection model for Euler-Euler and Euler-Lagrange large-eddy simulations of an evaporating spray inside an aeronautical combustor". *International Journal of Multiphase Flow,* ***37***(5), pp. 514–529.

[38] Prieur, K., 2017. "Combustion dynamics of an annular combustor with multiple spray injectors". Phd thesis, Université Paris Saclay.

[39] Paulhiac, D., Cuenot, B., Riber, E., Esclapez, L., and Richard, S., 2019. "Analysis of the spray flame structure in a lab-scale burner using large eddy simulation and discrete particle simulation". *Combustion and Flame,* ***212***, pp. 25–38.

[40] Franzelli, B., Riber, E., Sanjosé, M., and Poinsot, T., 2010. "A two-step chemical scheme for kerosene-air premixed flames". *Combustion and Flame,* ***157***(7), pp. 1364–1373.

[41] Smallbone, A. J., Liu, W., Law, C. K., You, X. Q., and Wang, H., 2009. "Experimental and modeling study of laminar flame speed and non-premixed counterflow ignition of n-heptane". *Proceedings of the Combustion Institute,* ***32***(1), pp. 1245–1252.

[42] Légier, J. P., Poinsot, T., and Veynante, D., 2000. "Dynamically thickened flame LES model for premixed and non-premixed turbulent combustion". *Proceedings of the Summer Program, Centre for Turbulence Research*, pp. 157–168.

[43] Charlette, F., Veynante, D., and Meneveau, C., 2002. "A power-law wrinkling model for LES of premixed turbulent combustion: Part I - non-dynamic formulation and initial tests". *Combustion and Flame,* ***131***, pp. 159–180.

[44] Rochette, B., Riber, E., Cuenot, B., and Vermorel, O.,

2020. “A generic and self-adapting method for flame detection and thickening in the thickened flame model”. *Combustion and Flame,* ***212***, pp. 448 – 458.

[45] Poinsot, T., and Lele, S., 1992. “Boundary conditions for direct simulations of compressible viscous flows”. *Journal of Computational Physics,* ***101***(1), pp. 104–129.

[46] Lancien, T., 2018. “Etude numérique de l’allumage diphasique de foyers annulaires multi-brûleurs”. Phd thesis, Université Paris Saclay.

[47] Lacaze, G., Richardson, E., and Poinsot, T., 2009. “Large eddy simulation of spark ignition in a turbulent methane jet”. *Combustion and Flame,* ***156***(10), pp. 1993–2009.